Influence of shear-thinning rheology on the mixing dynamics in Taylor-Couette flow

Neil Cagney[a,b] and Stavroula Balabani[a,*]

[a]Department of Mechanical Engineering, University College London, WC1E 6BT

[b]School of Engineering and Materials Science, Queen Mary University of London, London E1 4NS, UK

*Corresponding author: s.balabani@ucl.ac.uk

Abstract

Non-Newtonian rheology can have a significant effect on mixing efficiency, which remains poorly understood. The effect of shear-thinning rheology in a Taylor-Couette reactor is studied using a combination of Particle-Image Velocimetry and flow-visualisation. Shear-thinning is found to alter the critical Reynolds numbers for the formation of Taylor vortices and the higher order wavy instability, and is associated with an increase in the axial wavelength. Strong shear-thinning and weak viscoelasticity can also lead to sudden transitions in wavelength as Reynolds number is varied. Finally, it is shown that shear-thinning causes an increase in the mixing time within vortices, due to a reduction in their circulation, but enhances the axial dispersion of fluid in the reactor.

Symbols and Abbreviations

Symbols

d	[m]	Gap width
f_s	[s^{-1}]	Sampling frequency
f_{WVF}	[s^{-1}]	Frequency of wavy instability
G'	[Pa]	Storage modulus
G''	[Pa]	Loss modulus
k	[mPa s^n]	Consistency
L	[m]	Axial length of reactor
n	[-]	Flow index (Carreau model)
n_{PL}	[-]	Flow index (Power law model)
N_v	[-]	Number of vortices
r	[m]	Radius

1

r_i	[m]	Radius of inner cylinder
r_o	[m]	Radius of outer cylinder
t	[s]	Time
t_{visc}	[s]	Viscous time-scale
t_{mix}	[s]	Mixing time
z	[m]	Axial position

Greek symbols

$\dot{\gamma}$	[s^{-1}]	Strain rate
$\dot{\gamma}_{nom}$	[s^{-1}]	Nominal strain rate
$\langle \Gamma \rangle_z$	[m^{2}s^{-1}]	Mean vortex circulation
δ	[-]	Ratio of storage and loss moduli
η	[-]	Radius ratio
λ_z	[m]	Axial wavelength
λ_c	[s]	Carreau time-scale (Carreau model)
λ_r	[s]	Relaxation time
μ	[Pa s]	Viscosity
μ_0	[Pa s]	Viscosity at zero shear (Carreau model)
μ_∞	[Pa s]	Viscosity at infinite shear (Carreau model)
ρ	[kg m^3]	Density
ω_θ	[s^{-1}]	Vorticity in meridian plane
Ω	[rad s^{-1}]	Rotation speed of inner cylinder

Non-dimensional Groups

AR	[-]	Aspect ratio
Re	[-]	Reynolds number
Re_c	[-]	Critical Reynolds number
$Re_{c,2}$	[-]	Critical Reynolds number for Wavy Vortex Flow
$Re_{t,1}$	[-]	Reynolds number for first wavelength transition
$Re_{t,2}$	[-]	Reynolds number for second wavelength transition
t^*	[-]	Time non-dimensionalised with respect to viscous time-scale
t^*_{mix}	[-]	Mixing time non-dimensionalised with respect to rotation period
We	[-]	Weissenberg number

Abbreviations

PIV		Particle-Image Velocimetry

1. Introduction

Non-Newtonian fluids are encountered both in nature and industrial applications. Understanding the behaviour of non-Newtonian fluids has particular significance for many mixing applications, where spatial and temporal variations in viscosity can lead to uncertainty in the mixing time of the system. Various non-Newtonian phenomena such as shear-thinning, shear-thickening and viscoelasticity are known to affect the appearance and characteristics of flow instabilities, chaotic advection and turbulence that may be required for efficient mixing [1,2,3].

Shear-thinning is a feature of many complex fluids, including pastes, emulsions, gels and suspensions of solid particles and cells, and hence is of particular interest for mixing applications. In most mixing processes, energy is supplied to the fluid via a shear-stress (e.g. at a moving boundary such as an impeller blade) and this kinetic energy is then dissipated throughout the fluid to achieve mixing. In the case of a shear-thinning fluid, the applied shear-stress will reduce the local viscosity and promote high rates of local mixing, while material far from the applied stress will experience low strain rates and will therefore be characterised by high relative viscosity and slow mixing [4]. In the absence of a significant background flow, this may lead to the appearance of slow mixing regions and heterogeneity in the reactor, similar to the formation of caverns in yield stress fluids [5], significantly increasing the mixing time.

As a result of these issues, scale-up of processes involving non-Newtonian fluids can pose a major challenge. Much of the work in the literature on mixing of non-Newtonian fluids has focussed on viscoelasticity, in which the fluid stresses depend not just on the instantaneous strain rate (as in Newtonian fluids), but also on the magnitude of the strain (elasticity), as these fluids are known to undergo instabilities at very low inertia [6, 7]. However, there has been relatively little work examining the case of shear-thinning inelastic or weakly viscoelastic fluids.

The early study of Metzner and Otto [8] examined mixing of Newtonian and shear-thinning fluids in a stirred tank reactor and found that shear-thinning rheology increased the critical Reynolds number (non-dimensional impeller speed) for transition to turbulence and the power required for rapid mixing. More recent studies of mixing in stirred tanks by Fontaine et al. [9] and Cortada-Garcia et al. [10] showed that shear-thinning fluids were associated with greater spatial variations in mixing, the appearance of slow-mixing islands and pseudo-cavern formation surrounding the impeller blades.

There has been relatively little work examining mixing of shear-thinning fluids in other types of reactors or under generalised conditions, such that the fundamental role of shear-thinning in mixing processes could be identified. For example, it remains unclear under what conditions shear-thinning may promote or supress flow instabilities that drive unsteady mixing, or how the characteristics of these instabilities (wavelength, time-scales etc.) may depend on the rheology.

The flow of a fluid between two concentric cylinders, the inner of which is rotating, is known as Taylor-Couette flow and has been used as an ideal case to study a variety of fluid phenomena [11]. Taylor-Couette flow has a simple and clearly defined geometry and undergoes a series of well-studied flow instabilities [12], making it a powerful approach through which to study the effect of non-Newtonian rheology on mixing. The dynamics of shear-thinning fluids in Taylor-Couette reactors are also of practical significance, as the system is used in many industrial applications involving non-Newtonian fluids, including filtration [13], protein-shearing [14, 15], blood detoxification [16], liquid-liquid extraction [17], food processing [18] and as a bioreactor [19, 20,21]. In spite of its theoretical and practical significance, it has been noted by several researchers that there is a lack of experimental data examining Taylor-Couette flow of shear-thinning fluids [1,22,23,24].

The dynamics in a Taylor-Couette reactor are controlled by the rotational speed of the inner cylinder, Ω, which is non-dimensionalised as the Reynolds number, $Re = \rho \Omega r_i d / \mu$, where ρ and μ are the density and dynamic viscosity, respectively, r_i is the radius of the inner cylinder and d is the width of gap between the cylinders. At slow rotation speeds, the fluid experiences uniform shear across the gap between the cylinders, a condition known as Circular Couette Flow. At a

critical Reynolds number, Re_c, the centrifugal forces are no longer balanced by viscosity and the flow becomes unstable, leading to the formation of a series of alternating toroidal vortices [25] which is referred to as Taylor Vortex Flow. Further increases in Re lead to more instabilities, most notably the appearance of an azimuthal travelling wave (Wavy Vortex Flow), which causes the locations of the vortices to oscillate in the axial direction [26].

Mixing in Taylor-Couette reactors can be broadly divided into two processes; mixing within individual vortices (intra-vortex mixing) and mass transfer between neighbouring vortices (inter-vortex mixing). When Taylor-Couette flow is applied in a batch process, inter-vortex mixing is essential for homogenisation. However, it can also be applied in continuous processes by superimposing a weak axial flow, in which case the flow in referred to as Taylor-Couette-Poiseuille flow and inter-vortex mixing is no longer a requirement[27]. Intra-vortex mixing is controlled by the velocity gradients within vortices that continuously stretch and deform fluid [28,29] and has been shown to increase with Reynolds number and show a weak dependence on the wave state [28,29,30]. Desmet et al. [31] argued that each vortex can be modelled as two separate zones, an inner zone at the vortex core and an outer zone near the vortex boundaries. The inner zone is characterised by relatively slow mixing [28,32] and is thought to occupy approximately 40% of the total vortex volume [33].

In the Taylor Vortex Flow regime, the flow remains axisymmetric, and mixing between neighbouring vortices occurs only via diffusion. However, the breakdown of symmetry in Wavy Vortex Flow and the oscillation of the vortices causes significant mass transfer between vortices [26], leading to an increase in the intervortex mixing [34]. Ohmura et al. [30] found that the intervortex mixing depended on Reynolds number and viscosity, and was inversely proportional to the wavelength of the flow, λ_z. However, Dusting and Balabani [28] showed that even in Taylor Vortex Flow, the intervortex mixing time may be smaller than the intravortex mixing time, due to the inefficient mixing in the vortex core zone.

It is not clear how intra- or inter-vortex mixing are affected by non-Newtonian rheology, or how this will ultimately affect the overall efficiency of the Taylor-Couette reactor. This study aims to address these questions, by providing experimental measurements of the dynamics within Taylor-Couette flow of Newtonian and non-Newtonian fluids. The remainder of the paper is structured as follows; the following section describes the experimental system used, and the velocity measurements and flow visualisation method used to study the dynamics; Sections 3.1 and 3.2 present time-averaged and unsteady results of these approaches, respectively; the implications for mixing are discussed in Section 4; followed by some concluding remarks on the findings of this study.

2. Experimental Details

The experiments were performed in a custom-made Taylor-Couette reactor, described in detail elsewhere [28,35]. The test-section comprised a Teflon inner cylinder, spray-painted black to reduce reflections, and a thin-walled outer cylinder mounted between two acrylic blocks. In order to reduce optical distortion when viewing the flow in the reactor, the test-section was enclosed within a square chamber made of acrylic plates that was filled with the same working fluid as in the reactor. The radii of the inner and outer cylinders were $r_i = 21.2$ mm and $r_o =$

25.5 mm, respectively, leading to a radius ratio of $\eta = r_i/r_o = 0.83$, while the length of the cylinder axis was $L = 55.5$ mm, leading to an aspect ratio of $AR = L/d = 12.97$.

The inner cylinder was mounted on a drive shaft and connected to a stepper motor (Smart Drive Ltd). Its rotation was monitored using an optical encoder with a high resolution (2000 pulses per revolution), which allowed the rotational speed of the inner cylinder to be controlled to a high degree of accuracy [35].

Four working fluids were examined, which were composed of mixtures of deionised water, glycerol and xanthan gum, as detailed in Table 1. The working fluids were mixed using a high-shear mixer for several minutes to ensure that the xanthan gum was fully dispersed, and the shear rheology was measured at room temperature using a rotational ARES rheometer (TA Instruments, with a Couette geometry. The resulting flow curves are shown in Figure 2(a). Shear-thinning can be described accurately using the Carreau model

$$\mu(\dot{\gamma}) = \mu_\infty + (\mu_0 - \mu_\infty)(1 + (\lambda_c\dot{\gamma})^2)^{\frac{n-1}{2}}$$ [1]

where μ_0 is the viscosity at negligible shear rates, μ_∞ is the viscosity at very high strain rates, λ_c is the characteristic time-scale, $\dot{\gamma}$ is the strain rate and n is the flow index, with $n = 1$ for Newtonian fluids and $n < 1$ for shear-thinning fluids.

Many studies in the literature have used the power law model to describe a shear-thinning rheology:

$$\mu(\dot{\gamma}) = k\dot{\gamma}^{n_{PL}-1}$$ [2]

where k is the consistency and n_{PL} is the flow index found using this model (which is not always the same as that found using Equation 1). While the power law model was found to work well over a limited range of strain rates, it underestimated the viscosity at high strain rates and overestimates it at low strain rates. Nevertheless, in order to facilitate comparison of the data in the current study with previous work in the literature, the power law model was also applied to the rheological measurements.

The best fits of the Carreau and power law models to the rheological data are presented in Figure 2(a), with the various fitting parameters listed in Table 1. In order to define the Reynolds number, it is necessary to choose a reference viscosity. In this study, the nominal strain rate across the fluid layer

$$\dot{\gamma}_{nom} = \frac{\Omega r_i}{d},$$ [3]

was utilised in the Carreau model (Equation 1).

Fluid	1	2	3	4
Water:glycerol ratio	3:1	4.08:1	1:0	1:0
Xanthan conc.	0 g/L	0.291 g/L	0.507 g/L	0.843 g/L
n	1	0.68	0.52	0.38
μ_∞	2.2 mPa s	1.73 mPa s	0.935 mPa s	1.28 mPa s
μ_0	2.2 mPa s	13.6 mPa s	85.3 mPa s	966 mPa s
λ_c	n/a	0 s	1.28 s	7.49 s

n_{PL}	0.995	0.73	0.531	0.401
k	2.2 mPa s^n	16.4 mPa s^n	77.4 mPa s^n	267 mPa s^n
λ_r	~0 s	$\ll$ 6.28 ms	< 6.28 ms	2.65 s

Table 1: Rheological properties of the various fluids used in experiments, including the fitting parameters of the Carreau and power law models (Equations 1 and 2, respectively).

Oscillatory shear measurements were performed to assess the viscoelasticity of the fluids. An oscillatory strain with a maximum amplitude of 10% was applied to the fluid samples and the unsteady stress signal was measured. By decomposing this signal into the viscous stresses in phase with the strain rate (the loss modulus, G'') and the elastic stresses in phase with the strain (the storage modulus, G'), the phase shift between the applied strain rate and the resulting fluids stresses could be found as

$$\delta = \tan^{-1}\frac{G'}{G''}.$$ [4]

This can be used to characterise the rheology, with $\delta = 0$ for purely viscous fluids, $\delta = 90°$ for solids and $0 < \delta < 90°$ for viscoelastic fluids.

The variation in the phase lag with oscillation frequency is shown in Figure 2(b). The Newtonian fluid has $\delta \approx 90°$ implying that it behaves as a purely viscous fluid, while all three xanthan solutions exhibit some viscoelasticity, with the elastic behaviour tending to become more important at high frequencies. For two fluids ($n = 0.68$ and $n = 0.52$), $\delta > 45°$, implying the rheology is dominated by viscous effects, while for the most shear-thinning case ($n = 0.38$), the elastic effects become dominant for excitation frequencies greater than 2.5 rad/s. Thus, the fluids examined in this study span the Newtonian, shear-thinning and viscoelastic regimes.

The frequency, ω_r, at which the $\delta = 45°$ can be used to identify the relaxation time of a fluid, $\lambda_r = 2\pi/\omega_r$. For three of the fluids, Figure 2(b) indicates that the relaxation time is too small to be measured ($\lambda_r < 6.28$ s). However, in the case of the most shear-thinning fluid, the relaxation time is given by 2.65 s. The significance of the relaxation time is given by the Weissenberg number, $We = \lambda_r\dot{\gamma}_{nom}$, which represents the ratio of the relaxation time to the time-scale of the flow. For $We \ll 1$, viscoelastic effects can be neglected, while for $We \sim 1$ they are likely to play a significant role in the dynamics.

The experiments were performed by slowly accelerating the inner cylinder at a constant rate to reach a final speed, Ω_{max}, which is listed in Table 2, along with the corresponding maximum Reynolds number and Weissenberg number. For Fluids 1,2 and 3, the Weissenberg number is relatively low, and it is clear that when the flow becomes unstable at $Re \sim \mathcal{O}(10^2)$, the Weissenberg number is significantly less than 1, suggesting elasticity plays a minor role in this instability. However, for Fluid 4, the Weissenberg number is significantly larger and can be expected to play an important role in the dynamics.

Fluid	1	2	3	4
Ω_{max}	22.9 rad/s	45.9 rad/s	61.3 rad/s	99.9 rad/s
$d\Omega_{max}/dt$	0.013 rad/s²	0.025 rad/s²	0.031 rad/s²	0.05 rad/s²
f_s (PIV)	40 Hz	80 Hz	80 Hz	80 Hz

f_s (vis)	10 Hz	20 Hz	25 Hz	45 Hz
Re_{max}	1015	1044	996	1312
We_{max}	~0	≪ 1.4	< 1.9	1312

Table 2: Details of the PIV and flow visualisation (vis) experiments performed on the four fluids (details of which are provided in Table 1).

The experiments were performed by slowly accelerating the inner cylinder at a constant rate, as listed in Table 2. The non-dimensional acceleration rate, dRe/dt^* (where $t^* = t/t_{visc}$, and $t_{visc} = \mu/\rho d^2$ is the viscous time-scale) was minimised, such that $dRe/dt^* < 5.5$ at any point in the experiments to ensure that the flow behaved in a quasi-steady manner (i.e. the flow state was not affected by the inner cylinder acceleration rate). The choice of acceleration rate was a balance between the need to avoid unsteady effects and the requirement that the measurements were performed over a reasonable time-scale, such that viscous heating did not lead to significant temperature variations. Experiments typically lasted approximately 30 minutes, and temperature measurements of the fluid in the reactor immediately before and after the experiments indicated that the temperature change was less than $\pm 1.2℃$.

As the inner cylinder was slowly accelerated, the flow was characterised using two approaches: Particle-Image Velocimetry (PIV) and flow visualisation. Time-resolved PIV was used to measure the velocity field in the meridian plane over short time-periods at several intervals. For each measurement, the plane was illuminated using a pulsed Nd:Yag laser and 1024 image-pairs were acquired spanning the length of the reactor using a high-speed camera (Phantom Miro M340). Fluorescent particles with a mean diameter of 10 μm were used as tracers. The sampling rate was high (Table 2), such that the change in the speed of the inner cylinder over the course of each measurement was small and this data could be used to represent the flow at a fixed Re. The image-pairs were processed using a cross-correlation scheme with 50% window overlap. The PIV fields had a vector spacing of 16 x 16 pixels (approximately 10 vectors over the gap width). To facilitate comparison between different experiments, all velocity data was linearly interpolated onto a regular grid spanning $r/d = 0.1 - 0.8$ and $z/d = 0.1 - 12.8$ in steps of 0.1, where r is measured with respect to the inner radius (i.e. $r_i/d = 0$). In order to reduce the effects of diffraction due to the curvature of the outer cylinder, velocity data acquired for $r/d > 0.8$ were ignored.

The PIV measurements provided detailed flow information over a number of discrete Reynolds numbers; however, they could not capture the evolution of the dynamics and the transitions between flow regimes, which require continuous measurements over the duration of the experiments. This could be achieved using flow visualisation. Following the completion of the PIV measurements, a small quantity of anisotropic tracer particles (mica flakes) were added to the flow. The quantity was sufficiently small (a volume fraction of $< 10^{-4}$) so that they had a negligible effect on the fluid viscosity, which was confirmed by additional rheometer measurements. Mica flakes have a high aspect ratio and thus align with the flow, such that the variations of the scattered light can be used to visualise the distribution of shear and identify structures in the flow [36]. This approach has been used by several previous researchers to study transitions in Newtonian Taylor-Couette flow [37,38,39].

A white LED light source (SugarCUBE, Edmund Optics) was used to illuminate the flow and images were acquired of a narrow strip of the flow at the front of the reactor (as indicated in Figure 1) using the same high-speed camera employed for the PIV measurements. The

sampling rate used for each experiment is listed in Table 2. By determining the image at which a banded structure appears, due to the formation for Taylor vortices, the critical Reynolds number could be determined.

3. Results

3.1 Flow Fields

The critical Reynolds number at which the flow transitions from stable Circular Couette Flow to unstable Taylor Vortex Flow, was determined from the flow visualisation measurements, and is shown as a function of the flow index in Figure 3(a). In each case, when the system initially transitioned from Circular Couette Flow, the vorticity fields contained a series of vortices that were stable and stationary, and in no case were any phenomena observed that are characteristic of the elasticity controlled instabilities (e.g. isolated 'diwhirls' or unsteady ribbon or spiral vortices [40, 41]). This indicates that the shear-thinning rheology is modifying the inertia-controlled Taylor-Couette instability seen in Newtonian fluids (i.e. the transition to Taylor Vortex Flow), rather than causing the flow becoming unstable due to the viscoelasticity of the fluids.

In order to compare the current estimates of Re_c to those of previous studies in the literature, the critical Reynolds number is also shown as a function of the flow index calculated using the power law model in Figure 3(b). The results from the current study indicate that shear-thinning is associated with a reduction in Re_c. However, this effect is not monotonic; there is a reduction of approximately 40% at $n = 0.68$ relative to the Newtonian case, but as n is reduced further Re_c increases. This trend is consistent with the experimental study of Sinevic et al. [42] who examined a slightly smaller radius ratio reactor ($\eta = 0.7$) and found a sharp increase in Re_c near $n_{PL} = 0.45$; by $n_{PL} = 0.4$, Re_c was larger than that observed for the Newtonian fluid.

In contrast, the analytical work using linear stability theory of [23,43,44] all predict an approximately steady decline in Re_c with decreasing flow index. The discrepancy between the results of the experimental studies and those of the theoretical work is interesting and suggests that the power law model used in the analytical studies summarised in Figure 3 may not capture all the relevant physics occurring in the experiments. This may arise in part because analytical predictions of the critical Reynolds number generally assume an infinite length reactor, while all experiments are performed in finite-aspect ratio systems (the system of Sinevic et al. [42] had an aspect ratio of 9.9). However, it should be noted that Cole [45] found that the aspect ratio has a negligible effect on the critical Reynolds number for $AR > 8$ (for Newtonian fluids).

It is notable that in the current study the fluids in which the shear-thinning is associated with an increase in the critical Reynolds number (relative to the minimum Re_c observed near $n = 0.68$) are also characterised by moderate viscoelasticity, such that the elasticity and viscous moduli are of comparable magnitude (Figure 2(b)). Viscoelasticity was not considered in the analytical work of Caton [43], Jastrzębski et al. [44] and Alibenyahia et al. [23], while Sinevic et al. [42] noted the presence of viscoelasticity in their fluids, but did not quantify it. Therefore, viscoelasticity is a potential explanation for the differences in the predictions of the analytical studies of ideal power law fluids and the experimental results of real shear-thinning fluids.

In order to examine the effects of shear-thinning on the flow within the reactor, the vorticity fields calculated from the time-averaged velocity fields at $Re \approx 500$ for each fluid are shown in Figure 4. In the Newtonian case, six pairs of counter-rotating vortices are present, which are approximately evenly spaced. As the flow index is reduced, the number of vortices, N_v, is also reduced, corresponding to an increase in the axial wavelength, $\lambda_z/d = AR/2N_v$. By $n = 0.38$ four vortex-pairs are present, with $\lambda_z/d = 3.24$, compared to $\lambda_z/d = 2.16$ for the Newtonian case.

The variation in the wavelength with Re for each fluid is shown in Figure 5 (neglecting the data points in the Circular Couette Flow regime, where the wavelength is given by $\lambda_z/d = AR$). For $n > 0.38$, λ_z/d remains constant at the Reynolds number is increased beyond Re_c. However, in the weakly elastic case ($n = 0.38$), the flow undergoes two discontinuities, with λ_z/d transitioning from 3.24 to 2.59 at $Re = 99 - 152$, before reverting to 3.24 in the range $Re = 309 - 385$. As the vorticity fields in Figure 6(a-e) show, this corresponds to the creation of a new vortex pair ($Re \approx 99 - 152$) and the subsequent disappearance of a vortex pair ($Re \approx 309 - 385$).

This creation and destruction of vortex pairs is unlikely to be captured by PIV measurements which provide measurements over relatively short periods of time. Instead, these transitions can be examined in the flow visualisation measurements which are shown in Figure 7(a) and 7(b) for the Newtonian and weakly elastic case, respectively. The maps were formed by averaging each image to form a single column of pixels spanning the axis of the reactor, and compiling these columns to form a stack, where the Reynolds number (and time) increases along the horizontal axis of the figure and the vertical axis corresponds to the reactor axis.

For $Re < Re_c$, the maps are broadly uniform due to the absence of clear flow features other than the Ekman vortices at either end. As the flow becomes unstable at Re_c, the maps are characterised by a series of light and dark bands, which correspond to the various bands of shear caused by the vortices. In the Newtonian case, this banded structure remains uniform for all $Re < 1000$, indicating that there is little change in the position or size of vortices as Reynolds number is increased.

For the weakly elastic case, there is a sudden change at $Re_{t,1} = 147$, in which several of the light and dark bands shift in the axial direction. This is associated with a new dark band forming at $z/d \approx 11.5$, which corresponds to the creation of a new vortex pair. The vortex splitting event appears to be spontaneous, and it is followed by a gradual shifting in the positions of all vortices such that they revert to a broadly uniform spacing by $Re \approx 200$.

This is followed by another abrupt transition at $Re_{t,2} = 235$, where the dark band at $z/d \approx 9.5$ disappears, which corresponds to the destruction of the vortex pair via merging with neighbouring vortices. This process is again followed by a gradual re-organisation of the vortices to achieve an approximately uniform axial spacing.

The process of vortex pair creation and destruction is consistent with the PIV results shown in Figure 6. In the flow visualisation experiment, $Re_{t,1} = 147$, which is in agreement with the PIV experiments, where $Re_{t,1}$ occurred in the range $99 < Re < 152$. However, the flow visualisation experiment indicates that $Re_{t,2}$ occurs at 235, while the PIV measurements indicate that the transition occurs at a slightly higher Reynolds number range, $309 < Re < 385$.

Sudden transitions in the number of vortices in Taylor-Couette of Newtonian fluids have been documented in previous studies, arising due to the effect of the wavy instability, as increases in Re lead to an increase in the amplitude of the wavy instability and a gradual reduction in the number of vortices present [46,47]. However, to the best of the authors' knowledge, the process observed here, in which a vortex pair is created and shortly thereafter another pair is destroyed (i.e. λ_z has a non-monotonic dependence on Re) has not previously been observed. Furthermore, the splitting/merging of vortices did not occur while the wavy instability was present (as will be shown in the following section), and therefore appears to be distinct from that described in previous studies of Taylor-Couette flow of Newtonian fluids [46,47]. The Weissenberg numbers at which the transitions occurred (at $Re_{t,1}$ and $Re_{t,2}$) were much greater than unity ($We = 317$ and 428, respectively) and significantly higher than any values seen in the $n = 0.68$ and 0.52 experiments, where no such transition were observed, which suggests that the abrupt changes in wavelength are associated with viscoelastic effects.

The various vorticity fields in Figures 4 and 6 indicate that as well as inducing an increase in the wavelength, shear-thinning is also associated with a concentration of vorticity at the centre of vortex-pairs, i.e. points where the is a positive (red) vortex on the left and a negative (blue) vortex on the right. This corresponds to a jet of fluid moving radially outward from the inner cylinder. In contrast, the inward jets (which occurs at points where there is a negative vortex on the left and a positive vortex on the right) are associated with patches of weak vorticity.

n	$Re_{c,2}$ (PIV)	$Re_{c,2}$ (vis)	$f_{WVF}\left(\frac{2\pi}{\Omega}\right)$ (PIV)	$f_{WVF}\left(\frac{2\pi}{\Omega}\right)$ (vis)
1	$761 - 846$	826	1.14	1.14
0.6	$682 - 834$	824	0.895	0.878
0.45	$635 - 750$	664	0.884	0.881
0.38	>1005	>1005	n/a	n/a

Table 3: Critical Reynolds number and characteristic frequency for the Wavy Vortex Flow found using velocity measurements (PIV) and flow visualisation (vis).

3.2 Wavy Instability

The wavy instability allows mass transfer between vortices and controls inter-vortex mixing [29]. Table 3 lists the Reynolds number at which the transition to Wavy Vortex Flow occurred, $Re_{c,2}$, and the frequency of the instability, f_{WVF}, for each fluid, based on both the flow visualisation and PIV measurements. For the PIV measurements, the Fast Fourier Transform (FFT) was used to find the spectra of the axial velocity component at every point in the measurement plane; these spectra were then averaged (in order to reduce the influence of the choice of measurement site) and the maximum was taken to coincide with f_{WVF}. For the visualisation measurements, f_{WVF} was found as a function of Re by dividing the spatio-temporal maps into segment 256 data points in length and computing the average FFT for each segment. For the weakly elastic case, the wavy instability was not observed at any Reynolds number examined, indicating that $Re_{c,2} > 1005$. The flow index does not appear to have a consistent effect on the critical Reynolds number for the transition to Wavy Vortex Flow. There is strong agreement between the estimates of $Re_{c,2}$ and f_{WVF} found using the flow visualisation and PIV measurements, indicating that the transition to wavy flow is repeatable

and the absence of a clear relationship between n and $Re_{c,2}$ or f_{WVF} is not a consequence of uncertainty in the measurements.

The wavy instability can be visualised using the vorticity fields averaged in the radial direction, $\langle \omega_\theta \rangle_r$, which are shown in Figure 8 for ten cylinder rotation cycles at $Re \approx 1000$. The increase in wavelength and the changes in the distribution of vorticity as the fluid becomes more shear-thinning are again apparent. In the Newtonian case, the instability can clearly be seen as an oscillation in the axial position of the boundary between vortices at $z/d \approx 4.5$, 6.5 and 8.5, which correspond to inward jets (in this case, a vortex boundary with a positive vortex above and a negative vortex below). The other boundaries, near the end of the reactor and at the outward jets, do not exhibit significant oscillations. The weakly elastic case exhibits some waviness at a single outward jet near the top of the reactor, $z/d \approx 11.5$, but the instability is not apparent at any other location (and thus in Table 3 it is not treated as being unstable). In the intermediate cases ($n = 0.68$ and 0.52, Figures 8(b-c)), the wavy instability is clearly visible at a number of inward and outward jets. In some cases, e.g. at $z/d \approx 5.5$ in Figure 8(b)), the amplitude of the instability is significantly larger than that observed at any points in the Newtonian case. It is clear that the reduction in the flow index is not associated with a clear trend in terms of $Re_{c,2}$ or the amplitude of the wavy instability; this may be a consequence of the viscoelasticity of the strongly shear-thinning fluids, as was discussed earlier regarding the critical Reynolds number for the transition to Taylor Vortex Flow (Figure 3).

4. Implications for Mixing

The results presented in the previous sections have significant implications for both the intra- and inter-vortex mixing. The intra-vortex mixing occurs within vortices and therefore is controlled by the strength and size of the vortices, which are characterised by the mean (absolute) circulation of vortices along the reactor, $\langle \Gamma \rangle_z$, and the axial wavelength, respectively. The mixing time within a single vortex is known to be inversely proportional to mean (absolute) vorticity within that vortex [48, 49], which is given by

$$t_{mix} \sim \frac{2\langle \Gamma \rangle_z}{d\lambda_z},$$

where $d\lambda_z/2$ is the cross-sectional area of a single vortex. This can be expressed relative to the period of rotation of the inner cylinder to give a non-dimensional mixing time that is proportional to the intra-vortex mixing time:

$$t_{mix}^* = \frac{d\lambda_z \Omega}{4\pi \langle \Gamma \rangle_z}. \tag{5}$$

This can be calculated from the time-averaged PIV data, using area integration of the vorticity to find $\langle \Gamma \rangle_z$. The resulting estimates of the mixing time are presented as a function of Reynolds number for each of the four fluids in Figure 9. The intra-vortex time decreases sharply at the onset of Taylor Vortex Flow, before reaching an approximately constant value for Re greater than around 500. Shear-thinning is associated with an increase in the intra-vortex mixing time. This is summarised in Figure 10, which shows the average value of t_{mix}^* found for $Re > 500$, normalised by the value found for the Newtonian case. A reduction in the flow index

leads to a non-linear increase in the mixing time, such that by $n = 0.38$, it becomes 30% larger than the value for a Newtonian fluid.

The simple mixing model summarised in Equation 5 assumes constant mixing throughout each vortex. However, it is known from experiments that intra-vortex mixing is characterised by a fast mixing region and a slow mixing core [28,31,34]. The vorticity fields in Figures 4 and 6 indicate that shear-thinning fluids are associated with a concentration of vorticity along some vortex boundaries and a reduction in vorticity in the vortex core region, which is likely to lead to a further decrease in the mixing time in the fast mixing regions and a further increase in the mixing time in the slow regions. This will act to reduce the overall efficiency of intra-vortex mixing in shear-thinning fluids relative to the Newtonian case, for which almost all estimates of the mixing times of Taylor-Couette reactors have been derived [28,29,31,34].

The inter-vortex mixing is controlled by the wavy instability, which allows for mass transfer between vortices. In the absence of waviness, dispersion of a fluid along the reactor axis relies on diffusion to cross vortex boundaries, which is a relatively slow process [30,34]. Therefore, the inter-vortex mixing time is strongly dependent on the wavelength of the flow, because if the wavelength is large there are less vortex boundaries that must be traversed. Shear-thinning is associated with an increase in λ_z (Figure 5), implying that it will lead to a reduction in the inter-vortex mixing time.

The inter-vortex mixing is also strongly dependent on the amplitude of the wavy instability and how this varies along the reactor axis. The Newtonian map (Figure 8(a)) shows that the wavy instability has a non-negligible amplitude only at every second vortex boundary, corresponding to the locations of jets moving radially inwards (i.e. containing fluid with low angular momentum), as was also reported by Wereley and Lueptow [50] and Nemri et al. [34]. The latter study of Nemri et al. [34] found that this can lead to significantly larger time required for mass transfer between vortices separated by an outward jet relative to vortices separated by an inward jet. The map in Figure 8(a) also indicates that at the inward jets, the amplitude of the instability is not the same at all locations, tending to be largest near the axial centre of the reactor and smallest near the ends. In an industrial process, reactors may be required to disperse a product introduced at one end along the entire span of the fluid. In this case, the overall mixing time will be dependent on the largest inter-vortex mixing time between two neighbouring vortices in the reactor; therefore, even if the mixing time is greatly reduced for vortices separated by an inward jet (and not for those separated by an outward jet), this will at most lead to a reduction in the overall mixing time by a factor of two.

In contrast, the moderately shear-thinning vorticity maps in Figures 8(b) and 8(c) show that the wavy instability is now present at a number of both inward and outward jets, which will be associated with a significant reduction in the inter-vortex mixing time. Furthermore, the amplitude of the wavy instability at some points in the shear-thinning fluids (e.g. at $z/d \approx 5 - 7$) is larger than that observed at any location in the Newtonian fluid, indicating a further increase in the efficiency of the mass transfer between vortices. However, the amplitude of the wavy instability does not appear to vary smoothly in the axial direction; Figure 8(c) shows that the amplitude tends to be high for $z/d > 7$, but is relatively low near the centre of the reactor, $z/d = 5 - 7$. This variability is likely to lead to some uncertainy in the estimates of the mixing time in practice.

Finally, the wavy instability was not observed in the strongest shear-thinning case (Figure 8(d)), other than at a single jet at the top of the reactor. The absence of wavy flow may be a consequence of the non-monotonic effect of the flow index on $Re_{c,2}$. Alternatively, viscoelastic fluids in rotating flows are known to exhibit hoop stresses [xxx2]; these stresses may act to stabilise the flow with respect to the inertia-controlled wavy instability, because any waviness will increase the length of the closed streamlines surrounding the inner cylinder and will thus be opposed by the hoop stresses.

However, even in the absense of significant wavy instability at $n = 0.38$, the inter-vortex mixing time will be reduced relative to the Newtonian case due to the increase in the wavelength; the vorticity maps in Figures 8(a) and 8(d) show that in both cases there are six vortex boundaries with low or negligible amplitude waves, despite the clear dominance of Wavy Vortex Flow in the Newtonian fluid.

Overall it appears that shear-thinning enhances the efficiency of axial disperion or inter-vortex mixing through the combined effects of an increase in the wavelength and the appearance of the wavy instability at both inward and outward jets. However, these effects are mitigated by the non-monotonic effects of shear-thinning on the critical Reynolds number for the onset of the wavy instability, possibly due to viscoelasticity.

5. Conclusions

The flow of Newtonian and shear-thinning fluids in a Taylor-Couette reactor was studied using Particle-Image Velocimetry and flow visualisation, in order to gain insight into how non-Newtonian rheology affects mixing. The Reynolds number was slowly increased, spanning the Circular Couette Flow, Taylor Vortex Flow and Wavy Vortex Flow regimes. The PIV measurements provided detailed information on the flow dynamics over short time periods when the Reynolds number was approximately constant whereas the flow visualisation allowed the transitions between regimes to be examined.

Shear-thinning was found to induce a reduction in the critical Reynolds number for the onset of Taylor Vortex Flow. However, at low flow index (strongly shear-thinning), further decreases in n lead to an increase in Re_c. This was consistent with the experiments of Sinevic et al. [42], but was not predicted by various analytical works for power law fluids [23,43,44], which may be caused by the viscoelasticity of the fluids used in the experiments.

Shear-thinning was found to lead to an increase in the axial wavelength in Taylor Vortex Flow (i.e. a decrease in the number of vortices present). In the most shear-thinning case, which was weakly elastic, the wavelength varied as the Reynolds number was increased, with the transitions occurring via the sudden splitting and merging of vortices.

The flow index also had a non-monotonic effect on the critical Reynolds number for the onset of the wavy instability. For the Newtonian fluid, the amplitude of the wavy instability was negligible at the outward jets, while in the moderately shear-thinning fluids ($n = 0.68$ and 0.52), the wavy instability was observed at both inward and outward jets. At some points along the reactor axis, the amplitude of the instability was significantly larger than that observed in the Newtonian case at a similar Reynolds number; however, in the shear-thinning fluids, there were significant variations in the amplitude along the axis. The most shear-thinning case ($n =$

0.38), was not found to undergo the transition to wavy flow in the Reynolds number range examined ($Re = 0 - 1005$), which may be related to the greater viscoelasticity of the fluid.

Finally, the implications of the findings on the mixing behaviour were discussed. The intra-vortex mixing time was argued to scale with the inverse of the mean vorticity, and it was shown that shear-thinning led to an increase in the intra-vortex mixing time. This effect was expected to be enhanced by the spatial distribution of vorticity in the shear-thinning cases, which led to large regions of weak vorticity and increased the relative size of the slow-mixing vortex cores.

In contrast, shear-thinning was found to improve inter-vortex mixing by increasing the amplitude of the wavy instability in moderately shear-thinning fluids and by increasing the wavelength, such that there were less vortex boundaries that the fluid must cross to achieve homogeneity.

References

[1] Coronado-Matutti, O., P. R. Souza Mendes, and M. S. Carvalho. 2004. "Instability of Inelastic Shear-Thinning Liquids in a Couette Flow Between Concentric Cylinders." Journal of Fluids Engineering 126: 385-390.

[2] Groisman, A., and V. Steinberg. 1997. "Solitary vortex pairs in viscoelastic Couette Flow." Physical Review Letters 78: 1460-1463.

[3] Jenny, M., S. K. Richter, N. Louvet, S. Skali-Lami, and Y. Dossmann. 2017. "Taylor-Couette instability in thixotropic yield stress fluids." Physical Review Fluids 2.

[4] Niederkorn, T. C., and J. M. Ottino. 1994. "Chaotic mixing of shear-thinning fluids." AIChE Journal 40: 1782-1793.

[5] Coussot, P. 2014. "Yield stress fluid flows: A review of experimental data." Journal of Non-Newtonian Mechanics 211: 31-49.

[6] Groisman, A., and V. Steinberg. 2000. "Elastic turbulence in a polymer solution flow." Nature 405: 53-55.

[7] Groisman, A., and V. Steinberg. 2001. "Efficient mixing at low Reynolds numbers using polymer additives." Nature 410: 905 - 908.

[8] Metzner, A. B., and R. E. Otto. 1957. "Agitation of non-Newtonian fluids." AIChE Journal 3: 3-10.

[9]Fontaine, A., Y. Guntzburger, F. Bertrand, L. Fradette, and M. C. Heuzey. 2013. "Experimental investigation of the flow dynamics of rheologically complex fluids in a Maxblend impeller system using PIV." Chemical Engineering Research and Design 91: 7-17.

[10] Cortada-Garcia, M., W. H. Weheliye, V. Dore, L. Mazzei, and P. Angeli. 2018. "Computational fluid dynamic studies of mixers for highly viscous shear thinning fluids and PIV validation." Chemical Engineering Science 179: 133-149.

[11] Fardin, M. A., C. Perge, and N. Taberlet. 2014. ""The hydrogen atom of fluid dynamics" - introduction to the Taylor-Couette flow for soft matter scientists." Soft Matter 10: 3523-3535.

[12] Andereck, C. D., S. S. Liu, and H. L. Swinney. 1986. "Flow regimes in a circular Couette system with independently rotating cylinders." Journal of Fluid Mechanics 164: 155-183.

[13] Holeschovsky, U. B., and C. L. Cooney. 1991. "Quantitative description of ultrafiltration in a rotating filtration device." A.I.Ch.E. Journal 37: 1219-1226.

[14] Ashton, L., J. Dusting, E. Imomoh, S. Balabani and E. W. Blanch. 2009. "Shear-induced unfolding of lyzosome monitored in situ" Biophysical Journal 96 (10): 4231-4236.

[15] Hill, E. K., B. Krebs, D. G. Goodall, G. J. Howlett, and D. E. Dunstan. 2006. "Shear Flow Induces Amyloid Fibril Formation." Biomacromolecules 7: 10-13.

[16] Ameer, G. A., E. A. Grovender, B. Obradovic, C. L. Cooney, and R. Langer. 1999. "RTD analysis of a novel Taylor-Couette flow device for blood detoxification." A.I.Ch.E. Journal 45: 633-638.

[17] Vedantam, S., and J. B. Joshi. 2006. "Annular centrifugal contactors - A review." Chemical Engineering Research and Design 84: 522-542.

[18] Masuda, H., R. Hubacz, M. Shimoyamada and N. Ohmura. 2019. "Numerical simulation of sterilization processes for shear-thinning food in Taylor-Couette flow systems." Chemical Engineering and Technology 42(4): 1-19.

[19] Curran, S. J., and R. A. Black. 2004. "Quantitative experimental study of shear stresses and mixing in progressive flow regimes within annular-flow bioreactors." Chemical Engineering Science 59: 5859 − 5868.

[20] Kong, B., J. V. Shanks, and R. D. Vigil. 2013. "Enhanced algal growth rate in a Taylor vortex reactor." Biotechnology and Bioengineering 110: 2140-2149.

[21] Haut, B., H. Ben Amor, L. Coulon, A. Jacquet, and A. Halloin. 2003. "Hydrodynamics and mass transfer in a Couette-Taylor bioreactor for the culture of animal cells." Chemical Engineering Science 58: 777-784.

[22] Ashrafi, N. 2011. "Stability analysis of shear-thinning flow between rotating cylinders." Applied Mathematical Modelling 35: 4407-4423.

[23] Alibenyahia, B., C. Lemaitre, C. Nouar, and N. Ait-Messaoudene. 2012. "Revisiting the stability of circular Couette flow of shear-thinning fluids." Journal of Non-Newtonian Fluid Mechanics 183-184: 37-51.

[24] Escudier, M. P., I. W. Gouldson, and D. M. Jones. 1995. "Taylor vortices in Newtonian and shear-thinning liquids." Proceedings of the Royal Society of London A 449: 155-175.

[25] Taylor, G. I. 1923. "Stability of a viscous liquid contained between two rotating cylinders." Philosophical Transactions of the Royal Society of London A 223: 289-343.

[26] Akonur, A., and R. M. Lueptow. 2003. "Three-dimensional velocity field for wavy Taylor-Couette flow." Physics of Fluids 15: 947.

[27] Giordano, R. L. C., R. C. Giordano and C. L. Cooney. 2000. "Performance of a continuous Taylor–Couette–Poiseuille vortex flow enzymic reactor with suspended particles." Process Biochemistry 35: 1093–1101.

[28] Dusting, J., and S. Balabani. 2009. "Mixing in a Taylor-Couette reactor in the non-wavy flow regime." Chemical Engineering Science 64: 3103-3111.

[29] Nemri, M., S. Charton, and E. Climent. 2016. "Mixing and axial dispersion in Taylor-Couette flows: the effect of the flow regime." Chemical Engineering Science 139: 109-124.

[30] Ohmura, N., K. Kataoka, Y. Shibata, and T. Makino. 1997. "Effective mass diffusion over cell boundaries in a Taylor-Couette flow system." Chemical Engineering Science 52: 1757-1765.

[31] Desmet, G., H. Verelst, and G. V. Baron. 1996. "Local and global dispersion effects in Couette-Taylor flow - II. Quantitative measurements and discussion of the reactor performance." Chemical Engineering Science 51: 1299-1309.

[32] Rudman, M., G. Metcalfe, and L. J. W. Graham. 2008. "Nonmixing vortex cores in wavy Taylor vortex Flow." Physics of Fluids 20: 063602.

[33] Campero, R. J., and R. D. Vigil. 1997. "Axial dispersion during low Reynolds number Taylor-Couette flow: intra-vortex mixing effects." Chemical Engineering Science 52: 3303–3310.

[34] Nemri, M., S. Cazin, S. Charton, and E. Climent. 2014. "Experimental investigation of mixing and axial dispersion in Taylor-Couette flow patterns." Experiments in Fluids 55: 1769–1784.

[35] Imomoh, E., J. Dusting, and S. Balabani. 2010. "On the quasiperiodic state in a moderate aspect ratio Taylor-Couette flow." Physics of Fluids 22: 044103.

[36] Abcha, N., N. Latrache, F. Dumouchel, and I. Mutabazi. 2008. "Qualitative relation between reflected light intensity by Kalliroscope flakes and velocity field in the Couette-Taylor flow system." Experiments in Fluids 45: 85-94.

[37] Dutcher, C. S., and S. J. Muller. 2009. "Spatio-temporal mode dynamics and higher order transitions in high aspect ratio Newtonian Taylor-Couette flows." Journal of Fluid Mechanics 641: 85–113.

[38] Majji, M. V., S. Banerjee, and J. F. Morris. 2018. "Inertial flow transitions of a suspension in Taylor-Couette geometry." Journal of Fluid Mechanics 835: 936-969.

[39] Bahrani, S. A., C. Nouar, A. Neveu, and S. Becker. 2015. "Transition to chaotic Taylor-Couette flow in shear-thinning fluids." 22ème Congrès Français de Mècanique. Lyon.

[40] Groisman, A. and V. Steinberg. 1997. "Solitary vortex pairs in viscoelastic Couette flow." Physical Review Letters 78: 1460–1463.

[41] Baumertand, B. J. and S. J. Muller. 1999. "Axisymmetric and non-axisymmetric elastic and inertio-elastic instabilities in Taylor-Couette flow," Journal of Non-Newtonian Fluid Mechanics 83: 33-69.

[42] Sinevic, V., R. Kuboi, and A. W. Nienow. 1986. "Power numbers, Taylor numbers and Taylor vortices in viscous Newtonian and non-Newtonian fluids." Chemical Engineering Science 41: 2915-2923.

[43] Caton, F. 2006. "Linear stability of circular Couette flow of inelastic viscoplastic fluids." Journal of Non-Newtonian Fluid Mechanics 134: 148-154.

[44] Jastrzębski, M., H. A. Zaidani, and S. Wronski. 1992. "Stability of Couette flow of liquids with power law viscosity." Rheologica Acta 31: 264-273.

[45] Cole, J. A. 1976. "Taylor-vortex instability and annulus-length effects." Journal of Fluid Mechanics 75: 1-15.

[46] Park, K., and G. L. Crawford. 1982. "Deterministic transitions in Taylor wavy-vortex flow." Physical Review Letters 50: 343-346.

[47] Crawford, G. L., K. Park, and R. J. Donnelly. 1985. "Vortex pair annihilation in Taylor wavy-vorex flow." Physics of Fluids 28: 7-9.

[48] Anokur, A. and M. Lueptow. 2002. "Chaotic mixing and transport in wavy Taylor–Couette flow." Physica D 167: 183-196.

[49] Cetigen, B. M. and N. Mohamed. 1993. "Experiments on liquid mixing and reaction in a vortex." Journal of Fluid Mechanics 249: 391-414.

[50] Wereley, S. T., and R. . M. Lueptow. 1998. "Spatio-temporal character of non-wavy and wavy Taylor-Couette flow." Journal of Fluid Mechanics 364: 59-80.

[51] Esser, A., and S. Grossmann. 1998. "Analytic expression for Taylor-Couette stability boundary." Physics of Fluids 8.

Figures
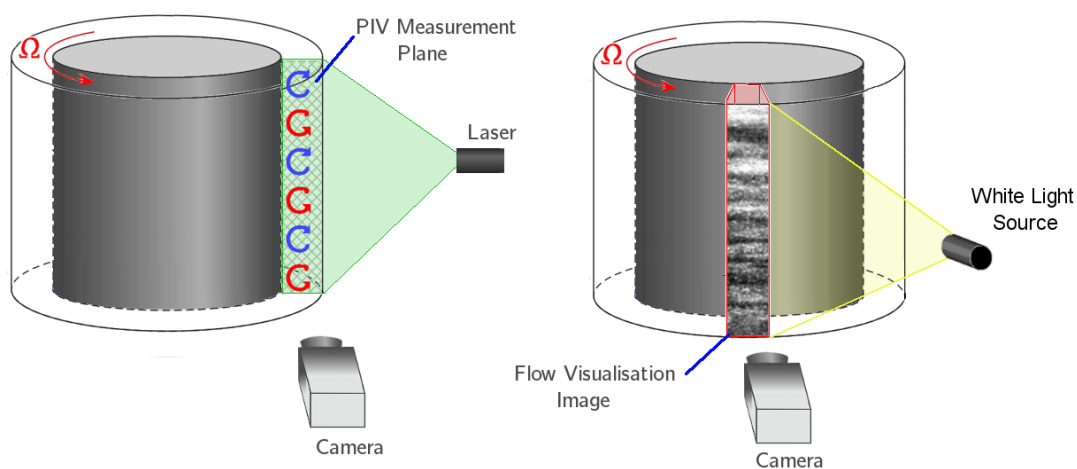
Figure 1: Sketch of the test-section used, showing the arrangement used to perform PIV (left) and flow visualisation measurements (right).
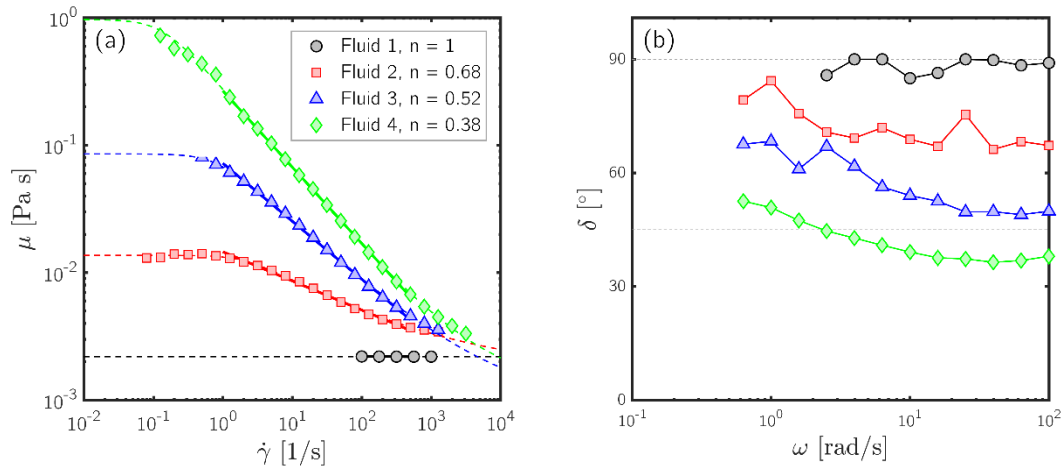

Figure 2: (a) Flow curves for the four fluids examined, including the best fit of the Carreau model (dashed lines) and the power law model (solid lines). The fitting parameters for both models are listed in Table 1 for each fluid. (b) Variation in the phase angle between the applied oscillating strain and the fluid stress (which provides a measure of the viscoelasticity of the fluid sample) with oscillation frequency.
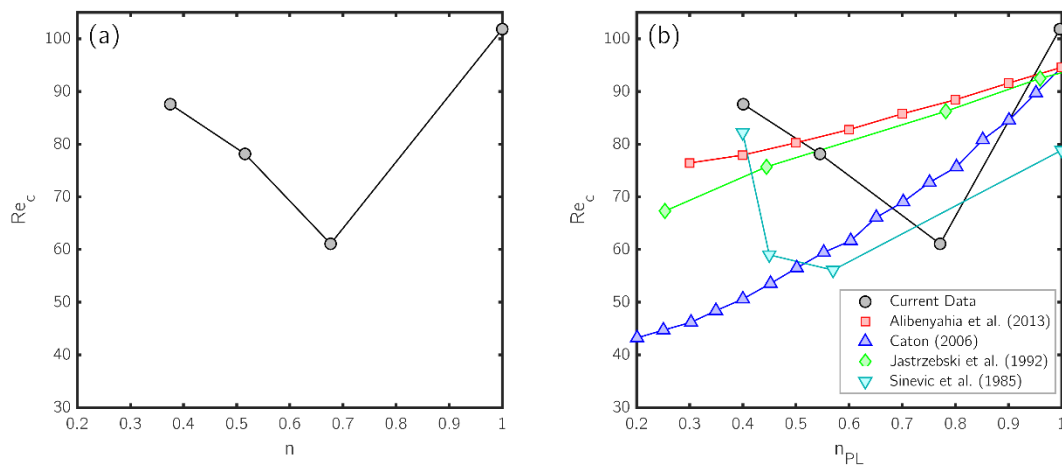
Figure 3: Variation in the critical Reynolds number for the onset of Taylor Vortex Flow as a function of flow index found using the Carreau model (a) and the power law model (b). The study of Sinevic et al. [42] was experimental, while the other studies summarised in (b) were analytical. The analytical studies were performed with a radius ratio of $\eta = 0.8$, while Sinevic et al. [42] used $\eta = 0.7$, which is responsible for the differences in Re_c found for the Newtonian case between these and the current work ($\eta = 0.83$) [51].
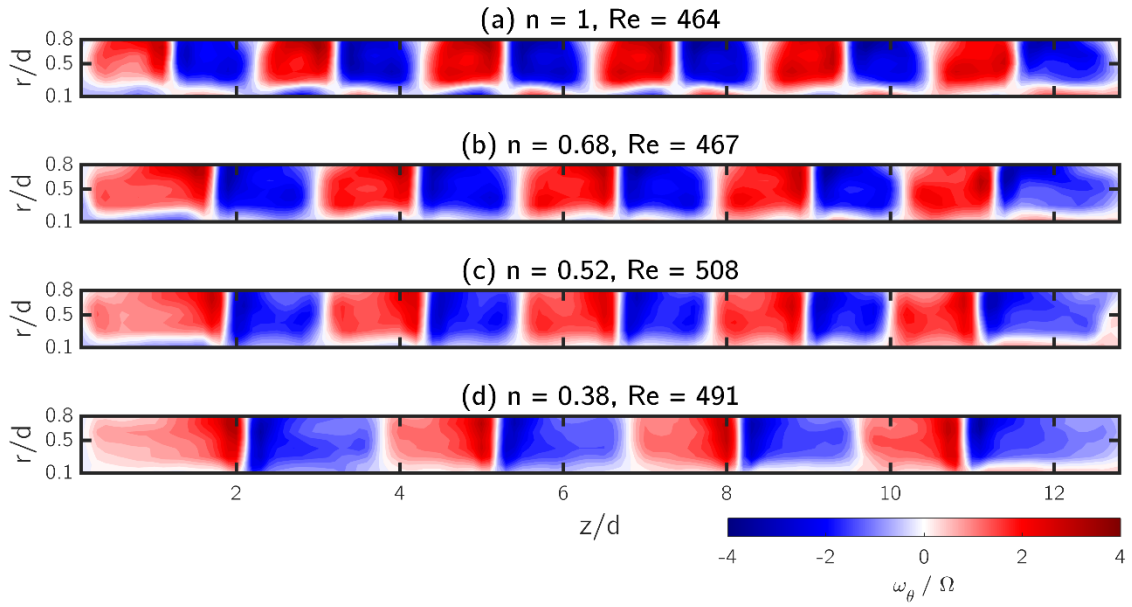
Figure 4: Vorticity fields, calculated from the mean velocity fields at $Re \approx 500$ for four fluids, including the Newtonian case (a), and three progressively more shear-thinning fluids (b-d).
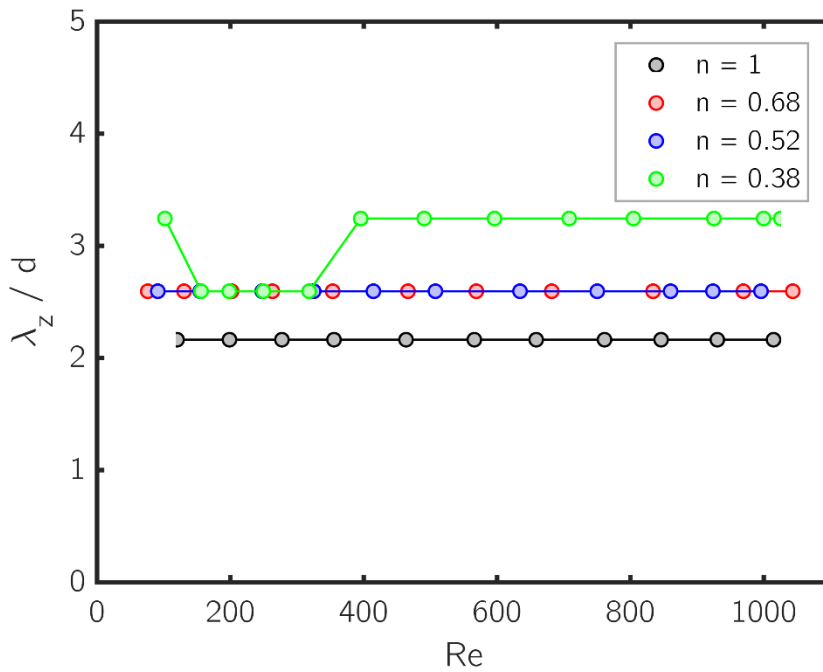

Figure 5: Variation in the mean wavelength of the flow with Reynolds number for four fluids. The sudden reduction in wavelength at $Re \approx 50 - 100$ corresponds to the formation of Taylor vortices.
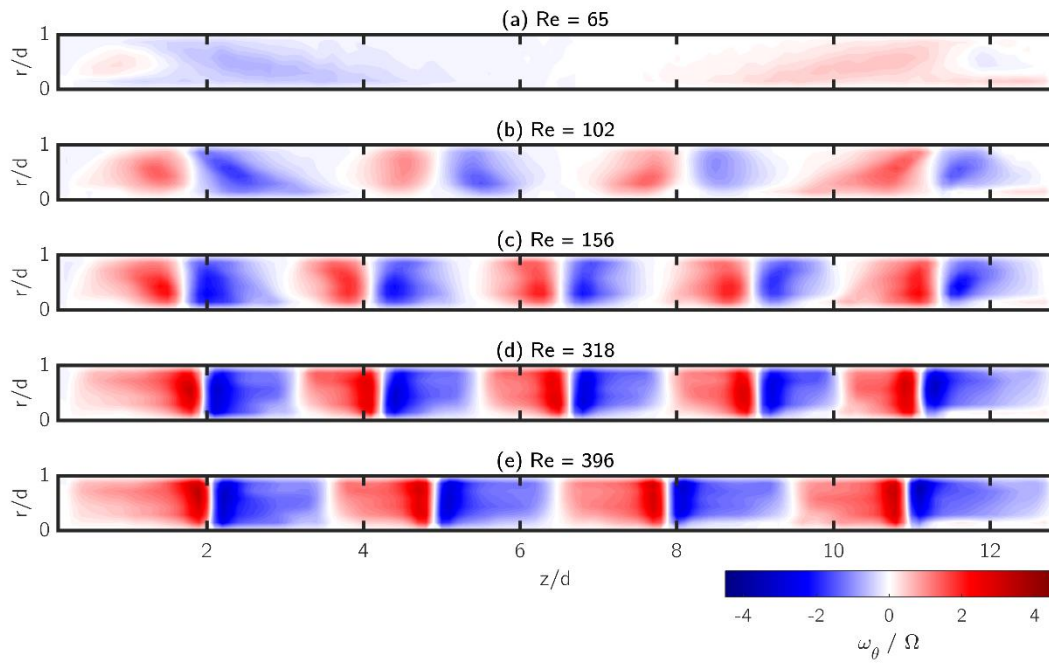
Figure 6: Vorticity fields acquired for the weakly elastic fluid ($n = 0.38$) at a range of Reynolds numbers, showing the transition to Taylor Vortex Flow (a-b), the increase in wavelength (b-c) and its subsequent decrease (d-e).
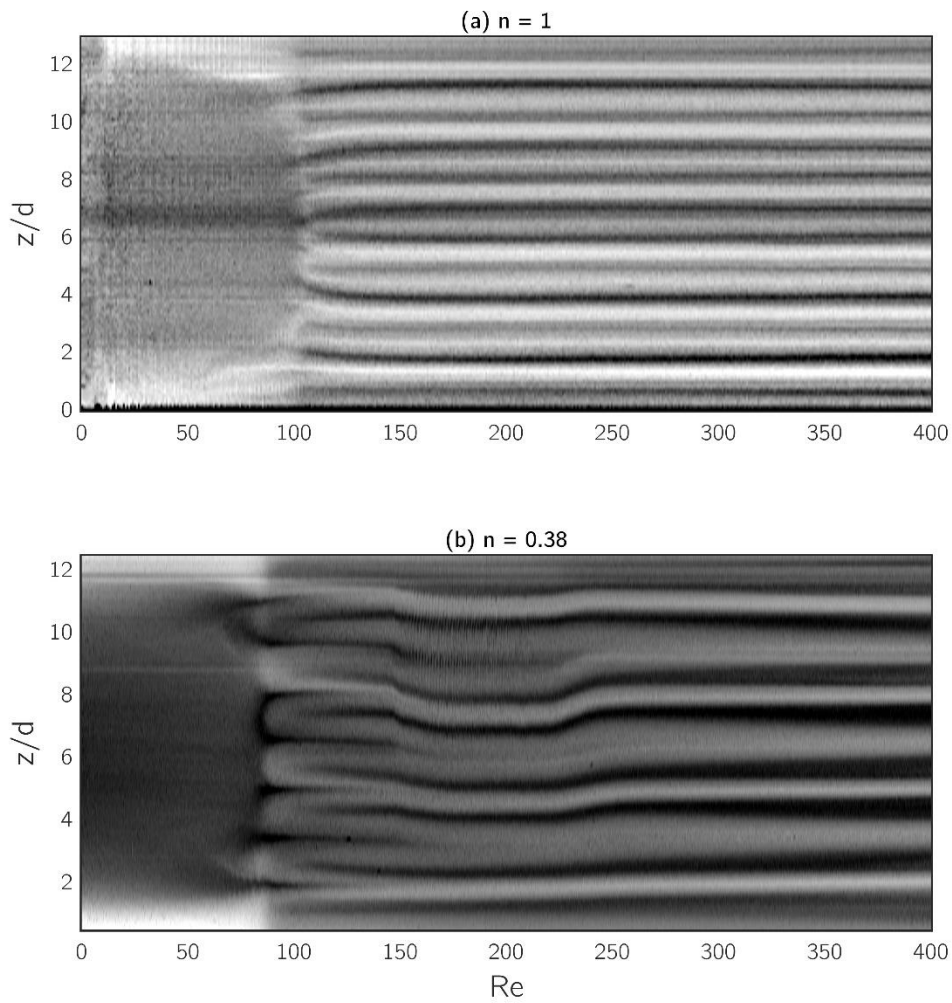
Figure 7: Flow visualisation maps acquired as the Reynolds number is gradually increased for a Newtonian (a) and strongly shear-thinning ($n = 0.38$) (b) fluid. Variations in intensity of the image correspond to changes in the local shear. The formation of horizontal bands at $Re \approx 100$ in (a) and ≈ 80 in (b) correspond to the transition to Taylor Vortex Flow. The shifts in the axial position of the bands in (b) in the region $Re = 120 - 250$ is caused by the formation of a new vortex pair at $z/d = 11.5$, followed by the destruction of another vortex pair at $z/d = 9.5$.
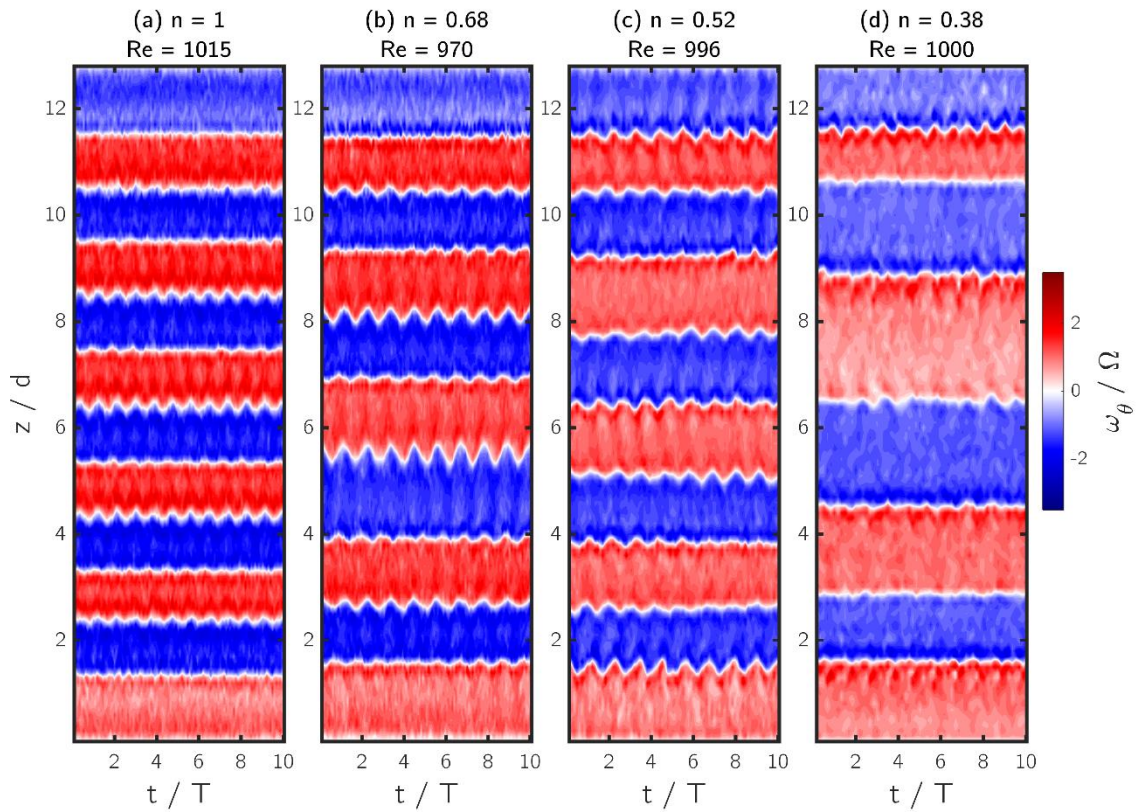
Figure 8: Radially averaged azimuthal vorticity over ten rotations of the inner cylinder for a Newtonian (a) and three shear-thinning (b-d) fluids at $Re \approx 1000$. The wavy instability can be seen as an oscillation of the boundaries of various vortices, but is not uniform throughout the reactor.
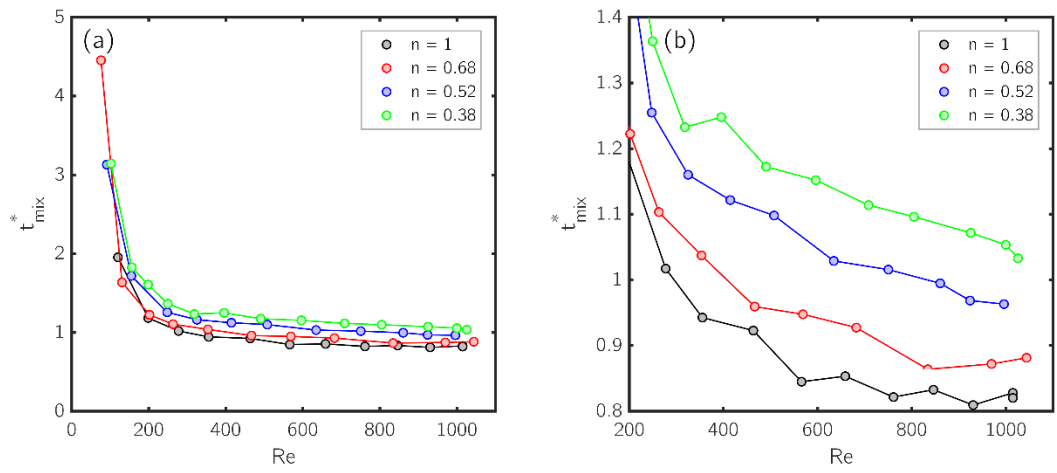

Figure 9: Variation in the non-dimensional mixing time for intra-vortex mixing (according to Equation 5) with Reynolds number for the four fluids (a). Mixing time decreases sharply at the

onset of Taylor Vortex Flow, after which shear-thinning tends to increase the mixing time. A close-up view of the trend lines in the plateau region for $Re > 200$ is shown in (b).
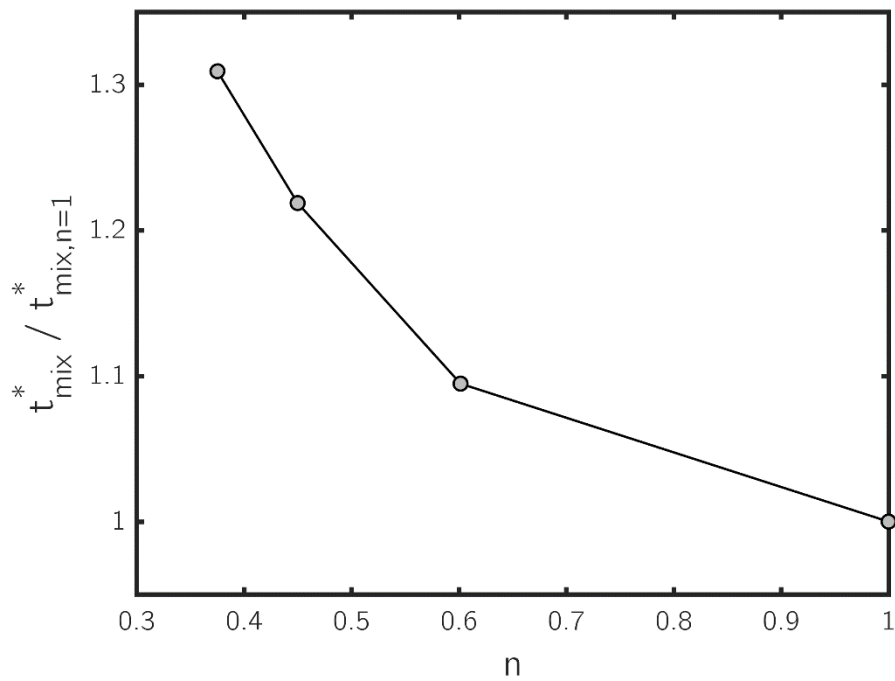

Figure 10: Variation in the mean estimate of the mixing time (found for PIV measurements acquired for $Re > 500$, using Equation 5) as a function of flow index. Results are normalised with respect to the predicted mixing time for the Newtonian case.